Deep SOAR follow-up photometry of two Milky Way outer-halo companions discovered with Dark Energy Survey

E. Luque,[1,2]★ B. Santiago,[1,2] A. Pieres,[1,2] J. L. Marshall,[3] A. B. Pace,[3] R. Kron,[4,5] A. Drlica-Wagner,[4] A. Queiroz,[1,2] E. Balbinot,[6] M. dal Ponte,[1,2] A. Fausti Neto,[2] L. N. da Costa,[2,7] M. A. G. Maia,[2,7] A. R. Walker,[8] F. B. Abdalla,[9,10] S. Allam,[4] J. Annis,[4] K. Bechtol,[11] A. Benoit-Lévy,[9,12,13] E. Bertin,[12,13] D. Brooks,[9] A. Carnero Rosell,[2,7] M. Carrasco Kind,[14,15] J. Carretero,[16] M. Crocce,[17] C. Davis,[18] P. Doel,[9] T. F. Eifler,[19,20] B. Flaugher,[4] J. García-Bellido,[21] D. W. Gerdes,[22,23] D. Gruen,[18,24] R. A. Gruendl,[14,15] G. Gutierrez,[4] K. Honscheid,[25,26] D. J. James,[27] K. Kuehn,[28] N. Kuropatkin,[4] R. Miquel,[16,29] R. C. Nichol,[30] A. A. Plazas,[20] E. Sanchez,[31] V. Scarpine,[4] R. Schindler,[24] I. Sevilla-Noarbe,[31] M. Smith,[32] M. Soares-Santos,[4] F. Sobreira,[2,33] E. Suchyta,[34] G. Tarle[23] and D. Thomas[30]

Affiliations are listed at the end of the paper

ABSTRACT

We report the discovery of a new star cluster, DES 3, in the constellation of Indus, and deeper observations of the previously identified satellite DES J0222.7−5217 (Eridanus III). DES 3 was detected as a stellar overdensity in first-year Dark Energy Survey data, and confirmed with deeper photometry from the 4.1-m Southern Astrophysical Research (SOAR) telescope. The new system was detected with a relatively high significance and appears in the DES images as a compact concentration of faint blue point sources. We determine that DES 3 is located at a heliocentric distance of $\simeq$76.2 kpc and it is dominated by an old ($\simeq$9.8 Gyr) and metal-poor ([Fe/H] $\simeq$ −1.84) population. While the age and metallicity values of DES 3 are comparable to typical globular clusters (objects with a high stellar density, stellar mass of $\sim 10^5$ $M_\odot$ and luminosity $M_V \sim -7.3$), its half-light radius ($r_h \sim 6.87$ pc) and luminosity ($M_V \sim -1.7$) are more indicative of faint star cluster. Based on the angular size, DES 3, with a value of $r_h \sim 0\!.'31$, is among the smallest faint star clusters known to date. Furthermore, using deeper imaging of DES J0222.7−5217 taken with the SOAR telescope, we update structural parameters and perform the first isochrone modelling. Our analysis yields the first age ($\simeq$12.6 Gyr) and metallicity ([Fe/H] $\simeq$ −2.01) estimates for this object. The half-light radius ($r_h \simeq 11.24$ pc) and luminosity ($M_V \simeq -2.4$) of DES J0222.7−5217 suggest that it is likely a faint star cluster. The discovery of DES 3 indicates that the census of stellar systems in the Milky Way is still far from complete, and demonstrates the power of modern wide-field imaging surveys to improve our knowledge of the Galaxy's satellite population.

Key words: globular clusters: general – Galaxy: halo.

1 INTRODUCTION

A fundamental prediction of the Lambda cold dark matter (ΛCDM) theory of structure formation is that galactic DM haloes of the size of the Milky Way (MW) grow by the accretion of smaller subsystems (e.g. White & Rees 1978; Davis et al. 1985; Font et al. 2011). The Sagittarius dwarf galaxy and the globular cluster Palomar 5 are interesting examples of physical systems that are even now going through the process of tidal disruption before being absorbed by the MW (see e.g. Ibata, Gilmore & Irwin 1994; Odenkirchen et al. 2002). Spectroscopic observations have shown that the dwarf

★ E-mail: elmer.luque@ufrgs.br

galaxies have central velocity dispersions larger than expected for baryonic material, assuming that the dwarf galaxies are dynamically relaxed stellar systems. It is widely accepted that dwarf galaxies are dominated by DM, with high dynamical mass-to-light ratios, while globular clusters typically do not exhibit evidence of DM (e.g. Mateo et al. 1993; Willman & Strader 2012; Ibata et al. 2013).

Based on the horizontal branch (HB) morphology, metallicity, structure, and kinematics, the globular clusters of the MW halo have been classified into two groups: the Young and Old Halo globular clusters (Zinn 1985, 1993). It is established observationally that the accretion of satellite galaxies leads to the accretion of globular clusters and possibly open clusters (e.g. Mackey & Gilmore 2004; Law & Majewski 2010; Marino et al. 2014, 2015). Direct evidence for this scenario is provided by the Sagittarius dwarf galaxy. By using the distance and radial velocity measurements of the stars of the Sagittarius stream and a sample of Galactic globular clusters, Law & Majewski (2010) determined that at least five globular clusters of the MW (Arp 2, M 54, NGC 5634, Terzan 8, and Whiting 1) originated in the Sagittarius dwarf. Additional evidence has been provided by Mackey & Gilmore (2004, and references therein). These authors compared the HB morphologies of the Young and Old Halo populations and the globular clusters of several satellite galaxies. They found that the globular clusters of the MW's satellites have HB morphologies similar to the Young Halo population. Therefore, searching for star clusters can help us understand the assembly history of our Galaxy and the associated globular cluster system.

With the advent of the Sloan Digital Sky Survey (SDSS; York et al. 2000), a new class of star clusters was discovered (e.g. Koposov et al. 2007; Belokurov et al. 2010; Fadely et al. 2011; Muñoz et al. 2012; Kim & Jerjen 2015a). These star clusters have very low luminosities ($-3.0 \lesssim M_V \lesssim 0$), small half-light radii ($r_\mathrm{h} < 10$ pc), and are thought to suffer mass-loss via dynamical processes such as tidal disruption or evaporation (see e.g. Koposov et al. 2007; Kim & Jerjen 2015a). The census of MW satellite galaxies has also increased considerably, from 11 classical dwarfs known in 1990, up to a total of 27 that were known by early 2015 (McConnachie 2012). Over the past three years many satellite candidates have been found in the following surveys: the Dark Energy Survey (DES; The Dark Energy Survey Collaboration 2005), the Panoramic Survey Telescope and Rapid Response System 1 (Laevens et al. 2014, 2015a,b), the Survey of the Magellanic Stellar History (Martin et al. 2015), VST ATLAS (Torrealba et al. 2016a,b), the Hyper Suprime-Cam Subaru Strategic Program (Homma et al. 2016, 2018), and the Magellanic SatelLites Survey (Drlica-Wagner et al. 2016). In particular, 21 stellar system candidates with $M_V \gtrsim -8$ have been found in DES (Bechtol et al. 2015; Drlica-Wagner et al. 2015; Kim & Jerjen 2015b; Koposov et al. 2015a; Luque et al. 2016, 2017). Thus far, spectroscopic measurements of radial velocity and metallicity have confirmed that Reticulum II (Koposov et al. 2015b; Simon et al. 2015; Walker et al. 2015), Horologium I (Koposov et al. 2015b), Tucana II (Walker et al. 2016), Grus I (Walker et al. 2016), Tucana III (Simon et al. 2017), and Eridanus II (Li et al. 2017) are indeed dwarf galaxies. The possible association of the recently discovered DES dwarf galaxy candidates with Large and Small Magellanic Clouds (LMC and SMC) has been discussed by several authors (e.g. Bechtol et al. 2015; Drlica-Wagner et al. 2015, 2016; Koposov et al. 2015a; Jethwa, Erkal & Belokurov 2016; Dooley et al. 2017; Sales et al. 2017). Several of the candidates may be associated with the Sagittarius stream (Luque et al. 2017).

Here, we announce the discovery of a new MW star cluster, which we call DES 3, in the constellation of Indus. The object was detected as a stellar overdensity in the first internal release of the DES co-add data (Y1A1), which covers a solid angle of $\sim$1800 deg^2 in the Southern equatorial hemisphere, and later confirmed with deep Southern Astrophysical Research (SOAR) imaging. We additionally present deeper imaging of DES J0222.7−5217 (Eridanus III) taken with the SOAR telescope in order to determine its properties, several of which have not been reported in the literature (Bechtol et al. 2015; Koposov et al. 2015a). We use these deeper data to better investigate the nature of this object, whether it be a star cluster or a very small faint dwarf. This paper is organized as follows. Section 2 describes the method used to search for star clusters and other stellar systems. In Section 3, we describe the first-year DES data and discovery of DES 3. The photometric follow-up observations and data reduction are presented in Section 4. In Section 5, we quantify the physical properties of the new stellar object. In Section 6, we present the updated properties of DES J0222.7−5217 with deeper imaging. Our final remarks are given in Section 7.

2 SUBSTRUCTURE SEARCH METHOD

Here, we briefly review our overdensity search technique (SPARSEX; Luque et al. 2016). The SPARSEX code is based on the matched-filter method (Rockosi et al. 2002; Szabo et al. 2011). It minimizes the variance between star counts from a data catalogue and a model containing a simple stellar population (SSP) and a MW field star contamination. This minimization is carried out over colour and magnitude bins for each individual and small spatial cell. A grid of SSPs covering a wide range of ages, metallicities, and distances, is created using the code GENCMD.[1] GENCMD uses PARSEC isochrones by Bressan et al. (2012) for different assumed distances and randomly selects stellar masses following a predefined initial mass function (IMF) from Kroupa (2001). The approach interpolates the stellar masses among the isochrone entries to draw absolute magnitudes in the desired filters. These are converted into measured apparent magnitudes using the assumed model distance, magnitude uncertainties taken from the Y1A1 data, and the reddening map of Schlegel, Finkbeiner & Davis (1998). The positions of the stars on the sky may also be simulated assuming different density profile models. To account for local variations in the field colour–magnitude diagram (CMD), we partition the sky into $10^\circ \times 10^\circ$ regions. The variance minimization yields the SSP model normalization as a function of position, i.e. a map with the number density of stars consistent with that particular SSP. We then convolve each SSP map with different spatial kernels to highlight substructures of different sizes. For each of these maps, we apply SEXTRACTOR (Bertin & Arnouts 1996) to identify the most significant and/or frequently detected overdensities. Then we perform visual inspection on the images, CMD, and significance profile of each candidate. The significance profile is defined as the ratio of the number of stars N_obj inside a given radius in excess of the number N_bgd, relative to the expected fluctuation in the same field background, i.e. $N_\mathrm{obj}/\sqrt{N_\mathrm{bgd}}$. Defining N_obs to be the total number of observed stars, then $N_\mathrm{obj} = (N_\mathrm{obs} - N_\mathrm{bgd})$. To avoid a low stellar statistic, we built the significance profile using a cumulative radius of $1'$ centred on the candidate. N_bgd is computed within a circular annulus at $30' < r < 36'$ from each candidate. We

---

[1] https://github.com/balbinot/gencmd

refer to Luque et al. (2016, 2017) and to Sections 3 and 5 below for more details.

3 DES DATA AND DISCOVERY

DES is a wide-field optical survey that uses the Dark Energy Camera (DECam; Flaugher et al. 2015) to image 5000 deg^2 in the Southern equatorial hemisphere. DECam is an array of 62 2k × 4k CCDs, with pixel scale of 0″.263, that images a 2°.2 diameter field of view. It is installed at the prime focus of the 4-m Blanco telescope at Cerro Tololo Inter-American Observatory. DECam images are reduced by the DES Data Management system. The pipeline consists of image detrending, astrometric calibration, nightly photometric calibration, global calibration, image coaddition, and object catalogue creation (see Sevilla et al. 2011; Desai et al. 2012; Mohr et al. 2012; Balbinot et al. 2015; Drlica-Wagner et al. 2018, for a more detailed description). The SEXTRACTOR toolkit is used to create catalogues from the processed and co-added images (Bertin & Arnouts 1996; Bertin 2011).

To search for stellar substructures in the DES Y1A1 catalogue, we applied cuts based on the SEXTRACTOR parameters SPREAD_MODEL, FLAGS and point spread function (PSF) magnitudes. The FLAGS parameter denotes if an object is saturated or has been truncated at the edge of the image and a cut of FLAGS < 4 is sufficient for our purposes. We apply this restriction in all our subsequent analyses. The SPREAD_MODEL parameter is the main star/galaxy separator. To avoid issues arising from fitting the PSF across variable-depth co-added images, we utilized the weighted-average (WAVG) of the SPREAD_MODEL measurements from the single-epoch exposures (see Bechtol et al. 2015). Therefore, our stellar sample consists of sources in the i band with |WAVG_SPREAD_MODEL| < 0.003 + SPREADERR_MODEL as described in Drlica-Wagner et al. (2015) and Luque et al. (2016). In addition, magnitude[2] ($17 < g_{DES} < 24$) and colour ($-0.5 < g_{DES} - r_{DES} < 1.2$) cuts were also applied. The colour cut was performed to exclude stars from the Galactic disc and possibly spurious objects that can contaminate our sample. Each star was extinction corrected from the reddening map of Schlegel et al. (1998).

Applying the method described in Section 2 on DES Y1A1 data, we have successfully recovered all 10 stellar objects that have been reported in first-year DES data[3] (Bechtol et al. 2015; Kim & Jerjen 2015b; Koposov et al. 2015a; Luque et al. 2016). These detections include the faint satellite DES J0222.7−5217, which we detect with significance of 16.1σ, where σ is the Poissonian standard deviation of the stars in the field of DES J0222.7−5217. Bechtol et al. (2015) reported DES J0222.7−5217 with a heliocentric distance of 95 kpc, an absolute magnitude $M_V = -2.4 \pm 0.6$, and a half-light radius of 11^{+8}_{-5} pc. In contrast, Koposov et al. (2015a) found DES J0222.7−5217 to be slightly less distant, 87 kpc, with an absolute magnitude $M_V = -2.0 \pm 0.3$, and a half-light radius of $14.0^{+12.5}_{-2.6}$ pc. Deeper imaging is necessary to conclusively determine the characteristics of this faint satellite.

In addition, to the previously detected satellites, we detected one new star cluster, DES 3, with a statistical significance of 8.3σ. DES 3 is readily visible as a cluster of faint blue stars in the DES co-add
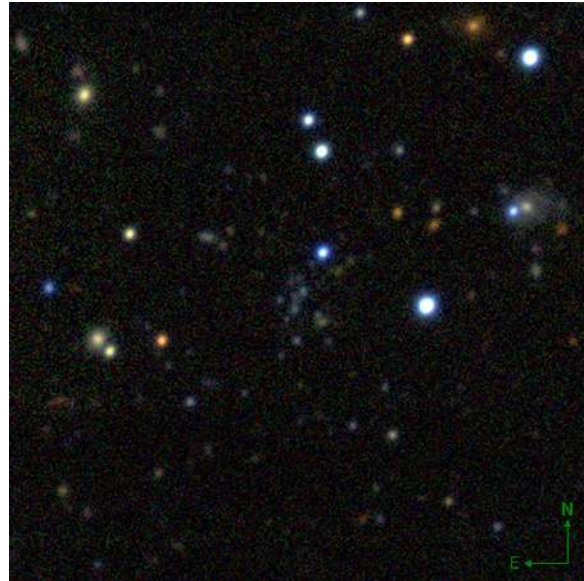

Figure 1. DES co-add image cutout of DES 3 taken from the DES Science portal. The 1′.58 × 1′.58 image is centred on DES 3. The R,G,B channels correspond to the i, r, g bands. North is up, and east is to the left.

images[4] (see Fig. 1). The fact that they are blue sources indicates that this overdensity is not a galaxy cluster. The overdensity is also clear from the DES stellar significance map shown in panel (a) of Fig. 2. The significance map, defined as $N_{cell}/N_{bgd}^{1/2}$, is built by subtracting the field stars (N_{bgd}) from the observed in a given spatial cell, N_{cell}, and dividing the result by the square root of the same field.[5] We replace negative values in the significance map by zero. For comparison, in panel (b), we show the significance map of sources classified as galaxies. Note that faint galaxies do not contribute to the observed overdensity of DES 3. In panel (c) of Fig. 2, the circular significance profile is shown. Note that the significance profile shows the higher peak at $r = 1'$ from the centre of DES 3, where $N_{obj} = 22$ and $N_{bgd} = 7$ stars. To take into account the missing coverage[6] observed in panels (a) and (b) of Fig. 2, in this analysis, we estimated the effective area (A_{eff}) for each circular region as follows. After inserting a certain number of uniformly distributed random points (N) inside a circle with radius r centred on DES 3, we computed the ratio between the number of points that fall inside the region of the sky covered by the DES data (N_{in}) and N. Therefore, for each region $A_{eff} = A \frac{N_{in}}{N}$, where A is the area of the circle.

In panel (d) of Fig. 2, we show the CMD of DES 3 constructed with stars within a circle of radius $r = 0'.64$, which is equivalent to two half-light radius (see Section 5 for details of the best-fitting

---

[2] We refer the WAVG_MAG_PSF measurements in the DES *gri* filters as g_{DES}, r_{DES}, and i_{DES}, respectively.

[3] The 11th object, Grus 1, reported by Koposov et al. (2015a) is in a region of Y1 data that is not included in the Y1A1 co-add due to limited coverage in some of the DES filters.
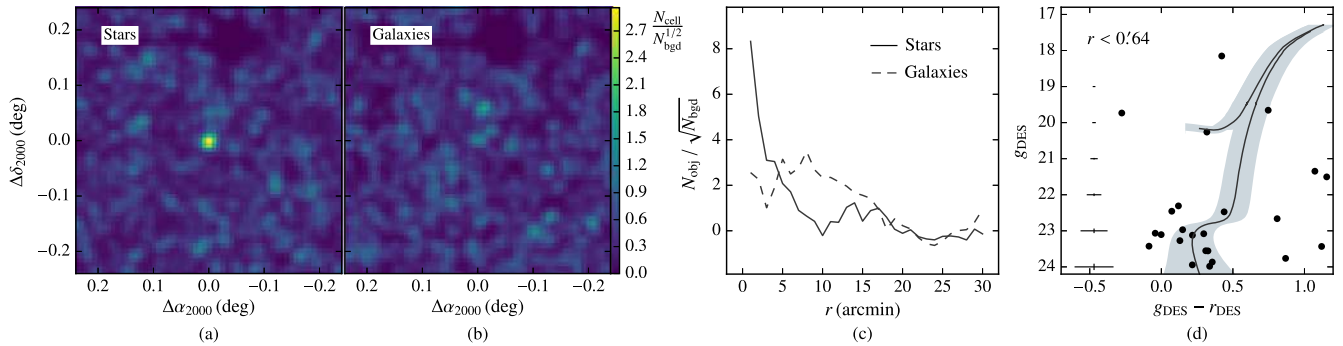
[4] The images were taken from the DES Science portal. The latter is a web-based system being developed by DES-Brazil and Laboratório Interinstitucional de e-Astronomia (LIneA, http://www.linea.gov.br) for the DES collaboration.

[5] N_{bgd} is computed with stars within a circular annulus at $30' < r < 36'$ from the centre of DES 3, weighted by the area of the spatial cell. The centre of DES 3 was determined from the best-fitting exponential profile (see Table 2).

[6] We masked the regions on the sky those were not covered by DES Y1A1 catalogue due to limited coverage in some of the DES filters, holes caused by CCD gaps, and the region affected by the very bright star located ∼11′.5 north-west of DES 3.

Figure 2. Detection of DES 3 from the DES data. Panel (a): stellar significance map built around DES 3 and smoothed by a Gaussian kernel with standard deviation $0\farcs5$. Panel (b): similar to previous panel, but now for galaxies [panels (a) and (b) share same colour bar]. Panel (c): significance profile as a function of radius r from the centre of DES 3. The solid line corresponds to stars, while the dashed line corresponds to galaxies. Panel (d): CMD of stars within a circle with radius $r = 0\farcs64$ from the centre of DES 3. A PARSEC (solid line) isochrone model with age 9.8 Gyr and [Fe/H] $= -1.84$ is overplotted at a distance of 76.2 kpc (see Section 5 for details of the best-fitting isochrone). The isochrone filter (grey shaded area) based on photometric uncertainties contains the most likely members. The mean photometric errors in both colour and magnitude are shown in the extreme left of this panel.

structural parameters). We also have plotted a PARSEC (CMD v3.0;[7] Bressan et al. 2012) isochrone model (solid line) corresponding to the best-fitting parameters (this will be discussed fully in Section 5). There are stars with $g_{\mathrm{DES}} \gtrsim 22.5$ scattered in the CMD, some of which fall inside the isochrone filter[8] (grey shaded area). We are tempted to say that these stars belong to the main sequence turn-off (MSTO) and subgiant branch (SGB) of DES 3. Note that the CMD also shows one star that may belong to the HB. However, based on the limited information given by this CMD, we are not able to confirm the nature and infer reliable parameters for DES 3. In order to reach the main sequence (MS; $g_{\mathrm{DES}} \sim 25.5$) in the CMD, deeper follow-up observations are required.

4 SOAR FOLLOW-UP DATA

Follow-up imaging of DES 3 and DES J0222.7−5217 was carried out on 2016 July 29 and October 20, respectively, using the SOAR Optical Imager (SOI) on the 4.1-m SOAR telescope. SOI consists of two 2048 × 4096 CCDs and covers a $5\farcm2 \times 5\farcm2$ field. The SOI CCDs have a scale of $0\farcs077$ pixel^{-1}. As the images were binned 2 × 2, the final image scale is $0\farcs154$ pixel^{-1}. We observed each object for a total of 45 min in each SDSS filter (g and r; hereafter g' and r'). The integrations were split into nine exposures of 300 s to avoid overexposing. The observations were carried out with an airmass below 1.20.

Raw exposures were trimmed, corrected for bias, and flat-fielded by the SOAR Brazilian Resident Astronomers, David Sanmartin, and Luciano Fraga, using SOAR/IRAF packages. Individual exposures for each filter, g' and r', were co-added. In particular, Fig. 3 shows the SOAR/SOI (g' band only) co-added images of DES 3. The figure attests to the increase in spatial resolution[9] and in photometric
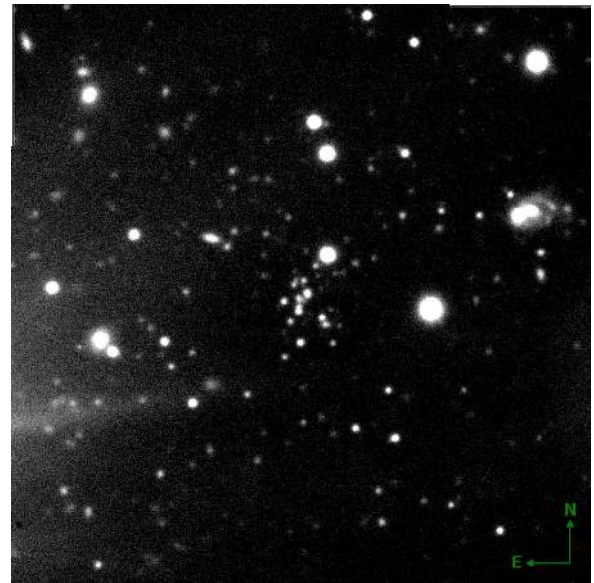

Figure 3. SOAR g- band co-add image cutout of DES 3. The $1\farcm58 \times 1\farcm58$ image is centred on DES 3. North is up, and east is to the left.

depth when the latter is compared with the DES images (see Fig. 1). The scattered light observed in Fig. 3 is discussed in the text below. To create a source catalogue in the direction of DES 3 and DES J0222.7−5217, we use a combination of the SEXTRACTOR/PSFEX routines (Bertin & Arnouts 1996; Bertin 2011). A first pass of SEXTRACTOR is run to create an input catalogue for PSFEX. The PSFEX routine creates a PSF image for a second pass of SEXTRACTOR that determines the PSF magnitude and the SPREAD_MODEL parameter.

We transformed the instrumental magnitudes, g_{inst} and r_{inst}, to apparent magnitudes,[10] g and r, by using a set of DES stars in the direction of each object. This process was performed as follows: first, we built a SOAR catalogue by merging the g' and r' full photometric lists, using a matching radius of $0\farcs5$. We also selected DES stellar sources with |WAVG_SPREAD_MODEL| < 0.003 and WAVG_MAGERR_PSF < 0.03 to obtain a sufficiently pure stellar

---

[7]We are using PARSEC isochrones revised to include instrumental and atmosphere response.

[8]The isochrone filter is built by using the photometric uncertainties in both colour and magnitude. We added a value of 0.1 mag in the colour–magnitude space to avoid too narrow isochrone filters at the bright magnitudes, where the uncertainties are small (for details, see Luque et al. 2016).

[9]By using several bright and isolated stars in the direction of DES 3, we determined that the DES co-added images have an average PSF FWHM of $\simeq 1\farcs19$ and $0\farcs94$ in the g and r bands, respectively, while the SOAR co-added images have a value of $\simeq 0\farcs8$ in both g' and r' bands.

[10]The g_{inst} and r_{inst} magnitudes are given by $-2.5 \times \log(\mathrm{counts})$, while the g and r magnitudes correspond to g_{DES} and r_{DES}, respectively.

Table 1. Calibration coefficients obtained from the fit of the set of equations presented in equation (1).

Coefficient	DES 3	DES J0222.7−5217
β (mag)	31.71 ± 0.02	31.43 ± 0.08
γ	-0.10 ± 0.02	-0.16 ± 0.09
ζ (mag)	31.70 ± 0.02	31.51 ± 0.03
η	-0.15 ± 0.03	-0.12 ± 0.02

sample. Next, we matched the SOAR sources with DES brightest (from 17 to 22 mag) stars, on g' and r' filters, using a radial tolerance of $0.''5$. Then, we use these brightest stars[11] to fit the following calibration curves:

$$g = g_{inst} + \beta + \gamma(g_{DES} - r_{DES}),$$
$$r = r_{inst} + \zeta + \eta(g_{DES} - r_{DES}), \quad (1)$$

where the β and ζ coefficients represent the zero-points of the two bands, while γ and η are the colour term coefficients. Airmass correction, in both filters, was assumed to be constant and therefore it is absorbed by the zero-point coefficient. The results of our fits are presented in Table 1. Estimates for the two objects are identical within uncertainties. The calibration was then applied to all instrumental magnitudes in the photometric list. Finally, all magnitudes of the calibrated sources were corrected for Galactic reddening using the Schlegel et al. (1998) dust maps, with typical reddening values $E(B-V) \simeq 0.019$ [$E(B-V) \simeq 0.025$] in the direction of DES 3 [DES J0222.7−5217].

For our further analysis, we modify the cuts to reach faint magnitudes. Our stellar sample consists of sources with |SPREAD_MODEL| < 0.003 + SPREADERR_MODEL. Moreover, we applied colour ($-0.5 < g_{DES} - r_{DES} < 1.2$) and magnitude ($g_{DES} > 17$) cuts. The faint g_{DES} magnitude, for each catalogue, is established based on the magnitude error (σ_g), where σ_g has a value of ≈ 0.07 mag. Therefore, this limiting magnitude corresponds to $g_{DES} < 25$ ($g_{DES} < 24.5$) for the star catalogue in the direction of DES 3 (DES J0222.7−5217).

We have verified that the scattered light observed only in the DES 3 images (see Fig. 3) does not affect the completeness of sources (stars and galaxies) down to a magnitude depth $g_{DES} \sim 25$. To check, we count sources as a function of magnitude both inside and outside scattered light affected regions. These regions have equal areas, which contain 159 and 154 sources, respectively. Thus, we find that both counts of sources in function of the magnitude are similar.

The completeness of our photometry has been evaluated performing artificial star tests on the SOAR images. The completeness curves are constructed with reference to the centre of each object up to an external radius $r = 1'$, taking regular intervals of $\Delta r = 0.''1$. Artificial stars from 20th to 27th magnitudes in steps of 0.5 mag were added to the same image with the IRAF/ADDSTAR routine using a PSF model derived from several bright and isolated stars. In order to avoid the crowding in the images, only 15 per cent of the original number of sources (stars and galaxies) detected in each region were added per run.[12] After inserting the artificial stars, these artificial images were reduced with the same SEXTRACTOR/PSFEX routines as the SOAR images. SEXTRACTOR/PSFEX assigns each detected object

[11]A total of 35 (23) stars were used for the photometric calibration of DES3 (DES J0222.75217).
[12]After multiple runs, we obtained a total of 120 artificial stars in each bin of magnitude.
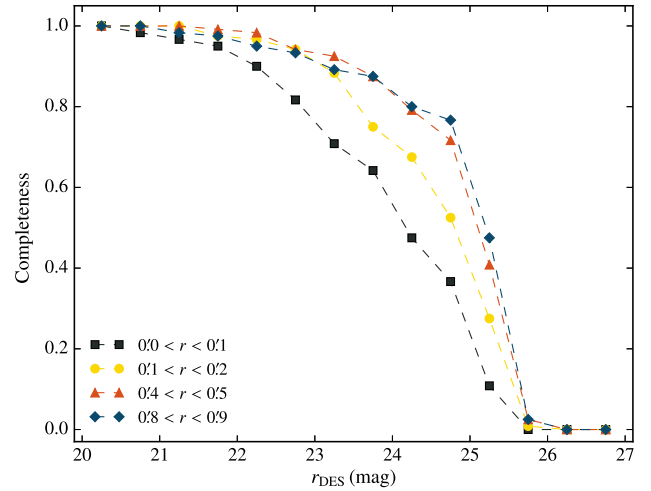

Figure 4. Completeness curves as function of magnitude and radius from the SOAR data. The solid squares represent the completeness at a radius of $0.''1$ from the centre of DES 3, the solid dots represent the completeness within an annulus with radius $0.''1 < r < 0.''2$, the solid triangles represent the completeness within an annulus with radius $0.''4 < r < 0.''5$, and the solid diamonds represent the completeness within an annulus with radius $0.''8 < r < 0.''9$.

Table 2. Properties of DES 3.

Parameters	Exponential profile	Plummer profile	Unit
α_0 (J2000)	$21\,40\,13.20^{+0.08}_{-0.08}$	$21\,40\,13.24^{+0.12}_{-0.12}$	h m s
δ_0 (J2000)	$-52\,32\,30.48^{+1.80}_{-1.80}$	$-52\,32\,30.48^{+1.80}_{-1.80}$	$\circ$ $'$ $''$
l	343.83	343.83	deg
b	-46.51	-46.51	deg
$D_\odot$	$76.2^{+2.5}_{-4.2}$	$76.2^{+2.8}_{-3.9}$	kpc
r_h	$0.32^{+0.05}_{-0.04}$	$0.30^{+0.05}_{-0.04}$	arcmin
r_h	$7.09^{+1.13a}_{-0.97}$	$6.65^{+1.13a}_{-0.95}$	pc
θ	$-10.72^{+38.33}_{-41.60}$	$-11.59^{+30.83}_{-32.18}$	deg
ϵ	$0.15^{+0.14}_{-0.11}$	$0.18^{+0.14}_{-0.12}$	
Σ_{bgd}	1.3 ± 0.2	1.3 ± 0.2	$\frac{stars}{arcmin^2}$
M_V	$-1.7^{+0.5}_{-0.3}$	$-1.6^{+0.5}_{-0.3}$	mag
[Fe/H]	$-1.84^{+0.18}_{-0.12}$	$-1.84^{+0.22}_{-0.12}$	dex
Age	$9.8^{+1.1}_{-0.9}$	$9.8^{+1.1}_{-1.1}$	Gyr
$(m-M)_0$	$19.41^{+0.07}_{-0.12}$	$19.41^{+0.08}_{-0.11}$	mag

[a]Adopting a distance of 76.2 kpc.

a SPREAD_MODEL value. We consider point source candidates those sources with |SPREAD_MODEL| < 0.003 + SPREADERR_MODEL (see the text above for details). At last, the artificial stars are considered to be recovered if the input and output positions are closer than $0.''5$, and magnitude differences are less than 0.5 mag. The completeness curves as a function of magnitude and distance from the centre of DES 3 are shown in Fig. 4.

5 PROPERTIES OF DES 3

In order to better constrain the properties and the nature of DES 3, we use SOAR data, which is ~1 mag deeper than the DES data in the region of this stellar object (see Fig. 3).
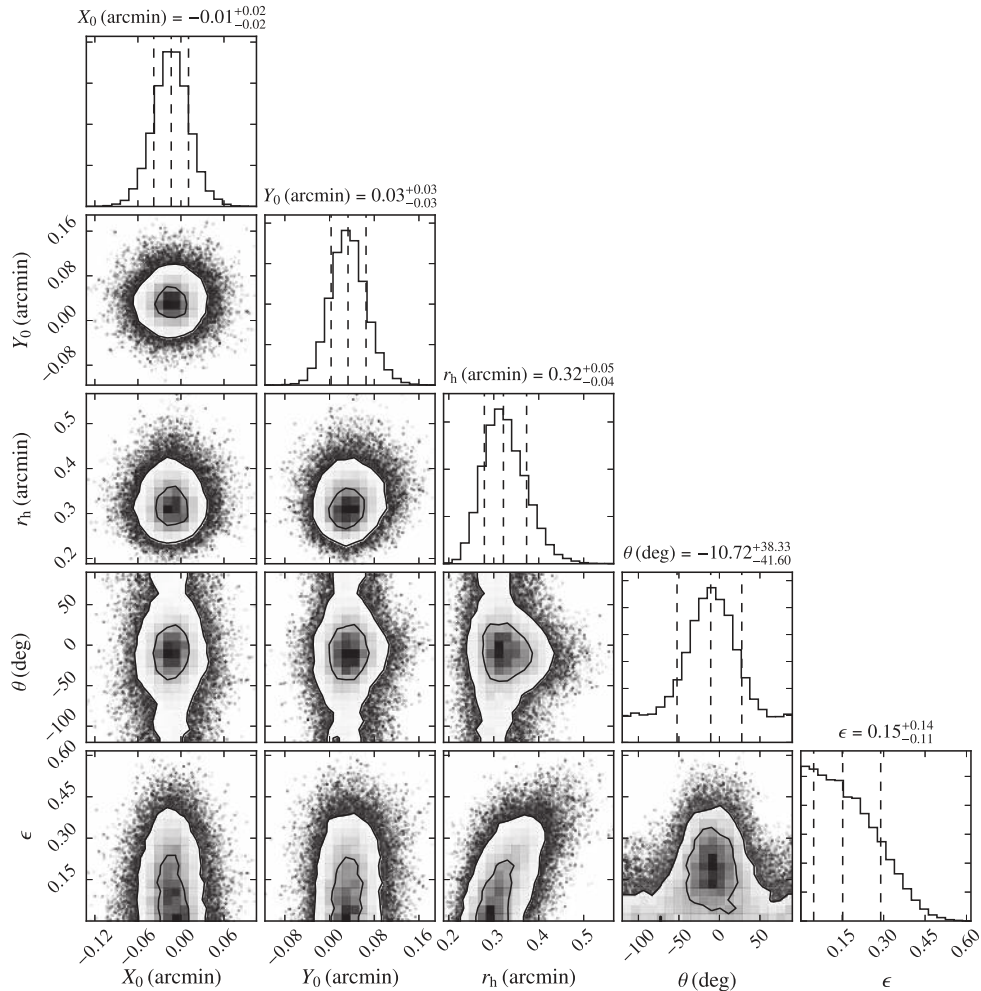
Figure 5. Marginalized PDFs for the structural parameters of DES 3 obtained from an exponential model. The vertical dashed central line represents the best-fitting solution, while the left (right) dashed line represents the uncertainty to -1σ $(+1\sigma)$. The contours show the 1σ and 2σ confidence levels. The coordinates of the centre of DES 3, $\alpha_0 = 21^h40^m13^s.20$ and $\delta_0 = -52°32'30''.48$, are determined by using the spatial offset of the centre, X_0 and Y_0, and the central coordinates obtained from a first run.

We use the maximum-likelihood method to determine the structural and CMD parameters for DES 3. We used the EMCEE[13] PYTHON package (Foreman-Mackey et al. 2013), which implements an affine invariant Markov Chain Monte Carlo (MCMC) ensemble sampler, to sample the ln–likelihood function over the parameter space. We have assumed flat priors for all parameters. We take the median of each marginalized posterior distribution function (PDF) to be the best-fitting solution, with uncertainties given by the 16th and 84th percentiles, equivalent to $\pm 1\sigma$ assuming the PDFs are normal distributions.

To estimate the structural parameters, we follow a convention similar to that of Martin, de Jong & Rix (2008). We adopt two different density profile models: exponential and Plummer (Plummer 1911). Due to the small field covered by the SOAR/SOI images, we parametrize both models with just five free parameters. For the exponential profile, the free parameters are central coordinates α_0 and δ_0, position angle[14] θ, ellipticity ϵ, and exponential scale radius r_e. For the Plummer profile, the parameters are α_0, δ_0, θ, ϵ, and Plum-

mer scale radius r_p. The exponential scale radius is related to the half-light radius by the relation $r_h = 1.68r_e$, whereas the Plummer scale radius, r_p, is equivalent to r_h.

First, we determine the best-fitting structural parameters using the method above described. For CMD fits, we first weight each star by the membership probability p taken from the first best profile fits. We then selected all the stars with a threshold of $p \geq 0.01$ to fit an isochrone model. The free parameters age, $(m - M)_0$ and metallicity,[15] Z, are simultaneously determined by this fitting method (Luque et al. 2016, 2017; Pieres et al. 2016). To investigate a possible range in the CMD parameters, in this analysis we use the selected stars from both exponential and Plummer models.

To reduce contamination by field stars in the determination of structural parameters, we use only stars that fall inside the isochrone filter [see panel (b) of Fig. 7]. Repeating the method to fit the structural parameters using the isochrone filter, we obtain the results shown in Table 2.[16] The background density, Σ_{bgd}, is determined

---

[13]http://dan.iel.fm/emcee/current/
[14]The position angle is oriented from north to east (Martin et al. 2008).

[15]We adopted $Z_\odot = 0.0152$ (Bressan et al. 2012) in order to convert from Z to [Fe/H], assuming [Fe/H] $= \log(Z/Z_\odot)$.
[16]We want to highlight that the lack of applying the isochrone filter would have increased the field density, but since there is an overdensity it does not
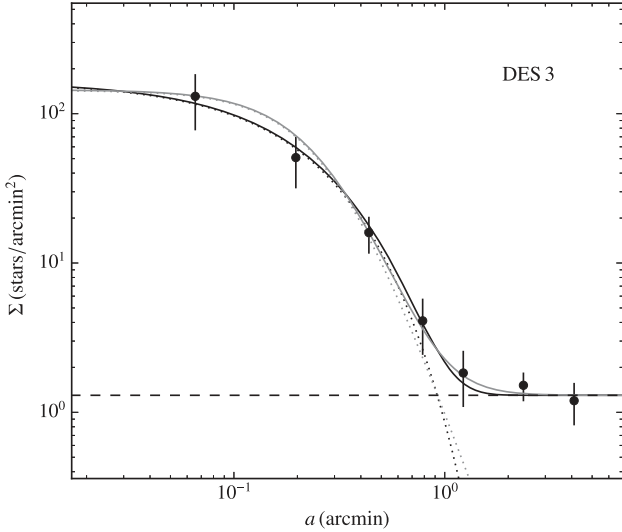
Figure 6. Filled points show a binned version of the density profile of DES 3, constructed in elliptical annuli using the derived structural parameters from the best-fitting exponential profile (see Table 2). The error bars are 1σ Poisson uncertainties. The grey (black) dotted line represents the best-fitting of Plummer (exponential) profile. The horizontal dashed line shows the field background level. The grey (black) solid line is the combination of the background level with the Plummer (exponential) profile.

by using a region outside $r > 1'.5$ around DES 3, which results in $1.3 \frac{\text{stars}}{\text{arcmin}^2}$, and it is kept constant in the fits. The resulting marginalized PDFs for the structural parameters obtained from the exponential model are presented in Fig. 5. Our MCMC run uses a total of 200 walkers and 800 steps including 300 steps for the burn-in phase.

Fig. 6 shows the binned elliptical density profile of DES 3. To determine the effective area of each elliptical annulus, correcting for the gap and borders of the field covered by the SOI CCDs, we follow the same technique used in Section 3. The best-fitting exponential and Plummer models are also overplotted in this figure. As it can be seen, both the exponential and Plummer profiles adequately describe the observed data. From both models, we find that DES 3 is only slightly elongated ($\epsilon \sim 0.17$) and compact, with a half-light radius of $r_h \sim 0'.31$. Its ellipticity is comparable to Kim 2 ($\epsilon \simeq 0.12$; Kim et al. 2015) and Kim 3 ($\epsilon \simeq 0.17$; Kim et al. 2016a). Only Koposov 1 and Koposov 2, with $r_h \sim 0'.21$ and $r_h \sim 0'.26$, respectively (Koposov et al. 2007), have slightly smaller angular sizes than DES 3.

Panel (a) of Fig. 7 shows the spatial distribution of all sources classified as stars with $g_{DES} < 25$ centred on DES 3, as obtained from the SOAR photometry. In panel (b) of Fig. 7, we show the CMD of DES 3 from the SOAR data. We show only stars within an ellipse with semimajor axis $a \simeq 2r_h$, $\theta = -10°.72$, and $\epsilon = 0.15$ according to the best-fitting exponential profile (see Table 2). This CMD clearly shows the presence of MS and SGB stars down to $g_{DES} \simeq 25.5$. We can also identify one star that may belong to the HB. In panel (c) of Fig. 7, we show the CMD of background stars contained in an elliptical annulus, centred on DES 3, of equal area as the previous panel, whose inner semimajor axis is equal to

generally affect the results significantly. In fact, we have obtained a variation of $\sim 0'.02$ on the half-light radius, ~ 0.02 on the ellipticity, and the angular position is within the uncertainties.

$a = 2'$. We used the technique described in Section 3 to determine the effective area of this region. The excess of stars within the isochrone filter seen in panel (b) relative to the background is remarkable, attesting not only the physical reality of DES 3, but also allowing a detailed CMD analysis. For comparison, in panel (d) of this figure, we show the CMD of DES 3 from the DES data [see panel (d) of Fig. 2]. As expected, the SOAR-based CMD is substantially more informative.

By using the maximum-likelihood method to fit the CMD distribution, we find that the DES 3 population is well described by a PARSEC (Bressan et al. 2012) isochrone model with age 9.8 Gyr, $(m - M)_0 \simeq 19.41$, and [Fe/H] $\simeq -1.84$. These parameters agree for both density profile models (exponential and Plummer). This is not surprising given that these models adequately describe the observed density profile of DES 3 (see Fig. 6). The best-fitting isochrone is overplotted in panels (b), (c), and (d) of Fig. 7 as the solid line. In the same figure, an isochrone filter (grey shaded area) is also shown in the last three panels.

The absolute magnitude (M_V) has been determined using a similar approach as Koposov et al. (2015a). We integrate over all masses along the best-fitting model isochrone assuming a Kroupa (2001) IMF, and normalize the number of objects by those observed in the CMD with $r_{DES} < 24.5$ and which fall in the isochrone filter built only with MS, MSTO, SGB, and red giant branch (RGB) stars. We corrected the star counts for completeness by weighting each star by $w_i = 1/c_i$, where c_i is the completeness of the star interpolated in magnitude for an interval of radius (see Fig. 4). In addition, we have also subtracted the expected number of field stars in the star counts as a function of magnitude. This was done as follows: first, we counted stars inside an ellipse of $3r_h$ semimajor axis from the centre of DES 3 and in a region limited by an ellipse with semimajor axis $a = 3'$, centred on DES 3, and the edges of the SOI CCDs. Then, we subtracted the star counts in the last region from the counts in the internal ellipse, weighted by their respective areas.[17] Due to the low number of stars observed in this type of objects, the estimate of the absolute magnitude has large uncertainty. We then calculate the uncertainty by estimating the upper and lower limits for the integrated V magnitude. We convert the g_{DES} and r_{DES} magnitudes to V magnitude using a SDSS stellar calibration sample[18] and the equation from Jester et al. (2005),

$$g_{DES} = g_{SDSS} - 0.075(g_{SDSS} - r_{SDSS}) + 0.001$$
$$r_{DES} = r_{SDSS} - 0.069(g_{SDSS} - r_{SDSS}) - 0.009$$
$$V = g_{SDSS} - 0.59(g_{SDSS} - r_{SDSS}) - 0.01. \quad (2)$$

This procedure yields an absolute magnitude of $M_V = -1.7^{+0.5}_{-0.3}$ for the exponential model and $M_V = -1.6^{+0.5}_{-0.3}$ for the Plummer model. Therefore, in the size–luminosity plane DES 3 lies in the faint star cluster region (see Fig. 8). The luminosity of DES 3 is comparable to Koposov 1 ($M_V \sim -2$; Koposov et al. 2007) and Gaia 2 ($M_V \simeq -2$; Koposov et al. 2017). However, the small size ($r_h \sim 6.87$ pc) of DES 3 is comparable to Balbinot 1 ($r_h \simeq 7.24$ pc; Balbinot et al. 2013), Kim 1 ($r_h \simeq 6.9$ pc; Kim & Jerjen 2015a), and Laevens 3 ($r_h \simeq 7$ pc; Laevens et al. 2015b).

---

[17]We have used the technique described in Section 3 to compute the effective area of each region.

[18]This new version of transformation equations are based on SDSS Data Release 13 (DR13) and DES Year 3 Annual Release (Y3A1) single-epoch data.
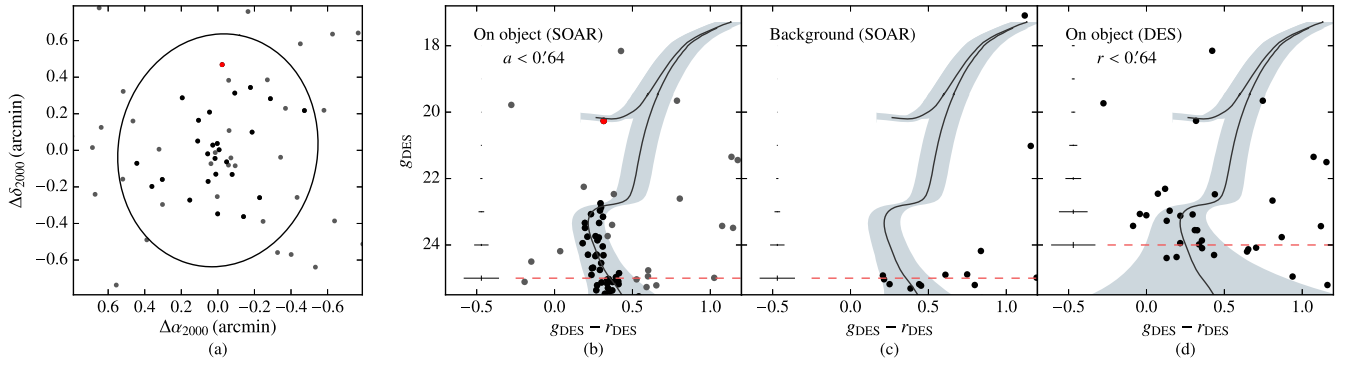
Figure 7. Panel (a): spatial distribution of all sources classified as stars, with $g_{DES} < 25$, from the SOAR data in a field of view of $1'.58 \times 1'.58$ centred on DES 3. The black dots represent the stars inside an ellipse with semimajor axis $a = 0'.64$ ($\simeq 2r_h$), $\theta = -10°.72$, and $\epsilon = 0.15$ (see Table 2), and that fall inside the isochrone filter as illustrated in the next panel. The red dot marks the possible HB star. Panel (b): CMD of DES 3 from the SOAR data. Only stars inside the ellipse marked on panel (a) are shown. In this and the other two panels, the best-fitting PARSEC (Bressan et al. 2012) isochrone derived from the SOAR data is shown. The isochrone filter (grey shaded area) based on photometric uncertainties contains the most likely members. Panel (c): CMD of field stars in an elliptical annulus, from the centre of DES 3, of equal area on the sky as the previous panel. Panel (d): CMD of DES stars within a radius $r = 0'.64$ centred on DES 3. The horizontal dashed line in the last three panels indicates the faint magnitude limit used. The mean photometric errors in both colour and magnitude are shown in the extreme left of panels (b), (c), and (d).
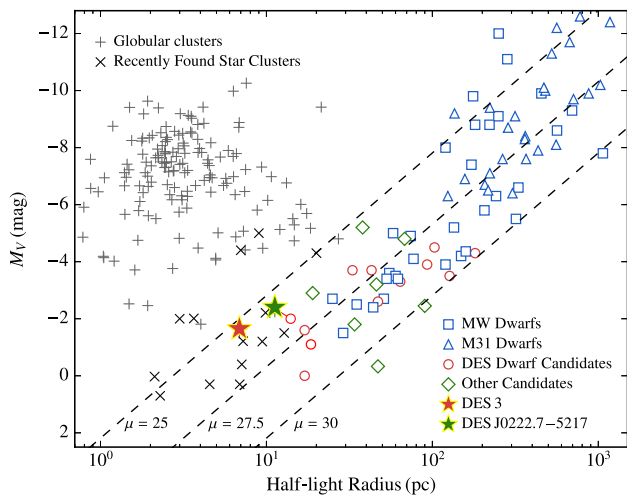
Figure 8. Absolute magnitude as a function of half-light radius. MW globular clusters ('+' symbols; Harris 2010), recently found MW star clusters ('×' symbols; Koposov et al. 2007; Belokurov et al. 2010; Muñoz et al. 2012; Balbinot et al. 2013; Laevens et al. 2014, 2015b; Kim & Jerjen 2015a; Kim et al. 2015, 2016a; Luque et al. 2016, 2017; Koposov, Belokurov & Torrealba 2017), MW dwarf galaxies (blue squares; McConnachie 2012; Bechtol et al. 2015, Drlica-Wagner et al. 2015; Koposov et al. 2015a; Kim et al. 2016b; Torrealba et al. 2016a,b), M 31 dwarf galaxies (blue triangles; McConnachie 2012), previously reported dwarf galaxy candidates in the DES footprint (red circles; Bechtol et al. 2015; Drlica-Wagner et al. 2015; Kim & Jerjen 2015b; Koposov et al. 2015a; Luque et al. 2017), other recently reported dwarf galaxy candidates (green diamonds; Laevens et al. 2015a,b; Martin et al. 2015; Drlica-Wagner et al. 2016; Homma et al. 2016, 2018), DES 3 (red star), and DES J0222.7−5217 (green star) are shown. The red circles connected with a line represent the two previous DES J0222.7−5217 estimates. Note that DES 3 and DES J0222.7−5217 lie inside the region inhabited by faint star clusters. The uncertainties of both objects are comparable to the symbol size. The dashed lines indicate contours of constant surface brightness at $\mu = \{25, 27.5, 30\}$ mag arcsec^{-2}.

6 PROPERTIES OF DES J0222.7−5217

As mentioned earlier, applying SPARSEX on DES Y1A1 data, DES J0222.7−5217 (first identified by Bechtol et al. 2015; Koposov et al. 2015a) was detected with a statistical significance that is close to 16 times the expected Poisson fluctuation in the background. Fig. 9 shows the same information as Fig. 2, but now for DES J0222.7−5217.

We obtained deeper photometric data for DES J0222.7−5217 with the SOAR telescope. Much like our SOAR imaging of DES 3, our SOAR imaging of DES J0222.7−5217 (see Fig. 10) is ~1 mag deeper than the DES data. We apply the same methodology described in Section 5 to provide updated properties of DES J0222.7−5217.

Fig. 11 shows the marginalized PDFs for the structural parameters of DES J0222.7−5217, and Fig. 12 shows the binned elliptical density profile of DES J0222.7−5217 and the best-fitting exponential and Plummer models. We find that the two models yield very similar structural parameters for this object (see Table 3). Our half-light radius ($r_h \simeq 0'.50$) estimate is ~16 per cent larger than the value determined by Bechtol et al. (2015, $r_h \simeq 0'.42$), but it is ~7 per cent smaller than that determined by Koposov et al. (2015a, $r_h \simeq 0'.54$). We find the system to be more elliptical ($\epsilon \sim 0.47$) and less rotated ($\theta \sim -76°$) when compared to the values previously determined ($\epsilon \simeq 0.27$ and $\theta \simeq -97°$; Koposov et al. 2015a). In general, our results are in agreement within 1σ with the literature. However, our deeper data have allowed us to better constrain the structural parameters of DES J0222.7−5217 thereby reducing significantly the uncertainties reported in previous work.

Panel (a) of Fig. 13 shows the spacial distribution of all stellar sources with $g_{DES} < 24.5$ in the vicinity of DES J0222.7−5217 obtained from the SOAR data. The CMD of DES J0222.7−5217 from the SOAR data is shown in panel (b) of Fig. 13. The CMD, built with stars within an elliptical annulus of semimajor axis $a \simeq 2r_h$ centred on the object, clearly shows MS, MSTO, blue straggler (BS), RGB, and HB stars. Note that there is a potential asymptotic giant branch (AGB) star. Panel (c) of Fig. 13 shows the CMD of field stars contained in an elliptical annulus, centred on DES J0222.7−5217, of equal area as the previous panel, whose inner semimajor axis
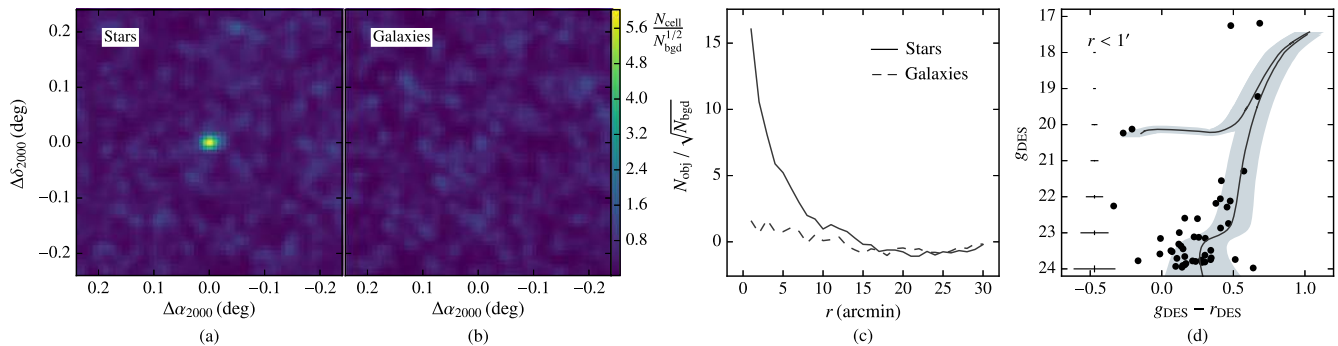
Figure 9. DES J0222.7−5217 from the DES data. Panel (a): stellar significance map built around DES J0222.7−5217 and smoothed by a Gaussian kernel with standard deviation 0.′5. Panel (b): similar to previous panel, but now for galaxies [panels (a) and (b) share same colour bar]. Panel (c): significance profile as a function of radius r from the centre of DES J0222.7−5217. The solid line corresponds to stars, while the dashed line corresponds to galaxies. Panel (d): CMD of stars within a circle with radius $r = 1'$ ($\simeq 2r_h$, see Table 3) from the centre of DES J0222.7−5217. A PARSEC (solid line) isochrone model with age 12.6 Gyr and [Fe/H] = −2.01 is overplotted at a distance of 77.3 kpc (see details in Section 6). The isochrone filter (grey shaded area) based on photometric uncertainties contains the most likely members. The mean photometric errors in both colour and magnitude are shown in the extreme left of this panel.
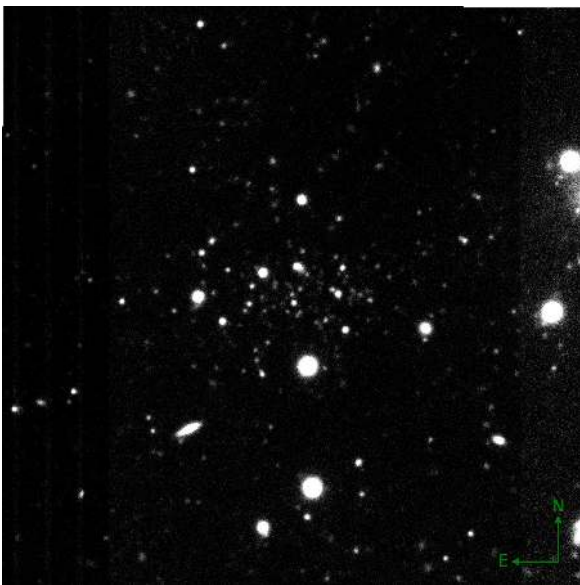
Figure 10. SOAR g-band co-add image cutout of DES J0222.7−5217. The $3' \times 3'$ image is centred on DES J0222.7−5217. North is up, and east is to the left.

is $a = 2.′5$. For comparison, in panel (d) of Fig. 13, we show the CMD of DES J0222.7−5217 from the DES data [see panel (d) of Fig. 9]. Only stars within a circle of radius $r = 1'$ from the centre of DES J0222.7−5217 are plotted. Much like SOAR data, this CMD shows BS, RGB, HB, and AGB stars; however, it does not provide enough information about the MSTO and MS stars. Therefore, the SOAR CMD is substantially more informative than the DES CMD.

The best-fitting model isochrone, determined from our CMD fit method, estimates that DES J0222.7−5217 is located at a distance of $D_\odot \simeq 77.3$ kpc and its stellar population is old ($\simeq 12.6$ Gyr) and metal poor ([Fe/H] $\simeq -2.01$). Again, the values of these parameters are consistent for both density profile models (see Table 3).

There is a moderate discrepancy between our heliocentric distance estimate and previous estimates of $D_\odot \simeq 95$ kpc (Bechtol et al. 2015) and $D_\odot \simeq 87$ kpc (Koposov et al. 2015a). In fact, this discrepancy may be due mainly to the limiting magnitude used in this work and those used by Bechtol et al. (2015) and Koposov

et al. (2015a), since the resolution of MS and MSTO allows for an improved distance measurement and estimations of the age and the metallicity. Unfortunately, the metallicity and age values were not reported by these authors.

We estimate an absolute magnitude for DES J0222.7−5217 of $M_V = -2.4^{+0.5}_{-0.3}$ for both density profiles. For these determinations, we used stars brighter than $r_{DES} = 24$ and the star counts were corrected for sample incompleteness, and subtracted the field stars. These results are in agreement (within 1σ) with those previously reported in the literature, $M_V \simeq -2.4$ (Bechtol et al. 2015) and $M_V \simeq -2.0$ (Koposov et al. 2015a).

With a half-light radius of $r_h \simeq 11.24$ pc and a luminosity of $M_V \simeq -2.4$, DES J0222.7−5217 lies in a region of size–luminosity space occupied by faint star clusters (see Fig. 8). Interestingly, the half-light radius, ellipticity, and absolute magnitude of DES J0222.7−5217 are comparable to those for the star cluster DES 1 ($r_h \simeq 9.88$ pc, $\epsilon \simeq 0.53$, and $M_V \simeq -2.21$; Luque et al. 2016).

7 CONCLUSIONS

In this paper, we announce the discovery of a new MW faint star cluster found in DES Y1A1 data, which we name DES 3. Its confirmation as a physical system required deep photometric imaging from the SOAR telescope. This new object adds to the 21 systems that have been found in the first two years of DES (Bechtol et al. 2015; Drlica-Wagner et al. 2015; Kim & Jerjen 2015b; Koposov et al. 2015a; Luque et al. 2016, 2017).

With a MCMC technique and two different density profile models (exponential and Plummer), we find that DES 3 is compact ($r_h \sim 0.′31$) and slightly elongated ($\epsilon \sim 0.17$). The nearly circular morphology of DES 3 does not suggest any evidence of on-going tidal disruption.

By means of an isochrone fit, we derive a distance of $\simeq 76.2$ kpc for DES 3. It is consistent with being dominated by an old ($\simeq 9.8$ Gyr) and metal-poor ([Fe/H] $\simeq -1.84$) population, as commonly observed in MW GCs found in the Galactic halo[19] [e.g. NGC 4833 ([Fe/H] $\simeq -1.85$) and NGC 5904 (age 10.0 ± 2.0 Gyr)]. However, its small physical size ($r_h \sim 6.87$ pc) and low luminosity

---

[19]For metallicities, see Harris (2010) and for ages, we refer to O'Malley, Gilligan & Chaboyer (2017) as a recent compilation.
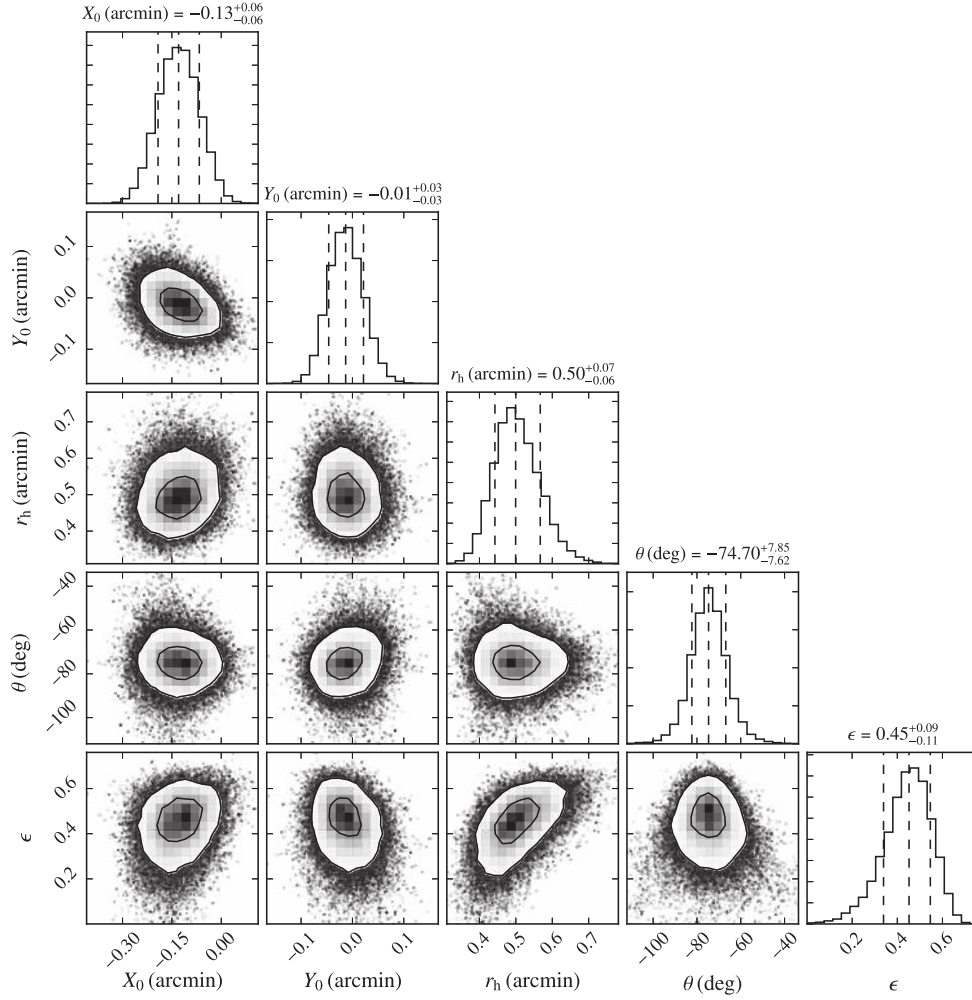
Figure 11. Marginalized PDFs for the structural parameters of DES J0222.7−5217 obtained from an exponential model. The vertical dashed central line represents the best-fitting solution, while the left (right) dashed line represents the uncertainty to -1σ ($+1\sigma$). The contours show the 1σ and 2σ confidence levels. The coordinates of the centre of DES J0222.7−5217, $\alpha_0 = 02^{\rm h}22^{\rm m}45\overset{\rm s}{.}48$ and $\delta_0 = -52°17'04\overset{''}{.}92$, are determined by using the spatial offset of the centre, X_0 and Y_0, and the central coordinates obtained from a first run.

Table 3. Properties of DES J0222.7−5217.

Parameters	Exponential profile	Plummer profile	Unit
α_0 (J2000)	$02\,22\,45.48^{+0.24}_{-0.24}$	$02\,22\,45.41^{+0.24}_{-0.24}$	h m s
δ_0 (J2000)	$-52\,17\,04.92^{+1.80}_{-1.80}$	$-52\,17\,05.64^{+1.80}_{-1.80}$	° ′ ″
l	274.96	274.96	deg
b	−59.60	−59.60	deg
$D_\odot$	$77.3^{+2.5}_{-3.9}$	$77.3^{+2.1}_{-4.3}$	kpc
$r_{\rm h}$	$0.50^{+0.07}_{-0.06}$	$0.50^{+0.07}_{-0.06}$	arcmin
$r_{\rm h}$	$11.24^{+1.62a}_{-1.46}$	$11.24^{+1.60a}_{-1.49}$	pc
θ	$-74.70^{+7.85}_{-7.62}$	$-76.80^{+7.45}_{-7.15}$	deg
ϵ	$0.45^{+0.09}_{-0.11}$	$0.48^{+0.09}_{-0.11}$	
$\Sigma_{\rm bgd}$	1.2 ± 0.2	1.2 ± 0.2	$\frac{\rm stars}{\rm arcmin^2}$
M_V	$-2.4^{+0.5}_{-0.3}$	$-2.4^{+0.5}_{-0.3}$	mag
[Fe/H]	$-2.01^{+0.43}_{-0.14}$	$-2.01^{+0.46}_{-0.14}$	dex
Age	$12.6^{+0.6}_{-0.9}$	$12.6^{+0.6}_{-1.2}$	Gyr
$(m - M)_0$	$19.44^{+0.07}_{-0.11}$	$19.44^{+0.06}_{-0.12}$	mag

^{a}Adopting a distance of 77.3 kpc.

($M_V \sim -1.7$) place DES 3 in the region occupied by faint star clusters as observed in Fig. 8. In fact, DES 3 is also one of the faint star clusters with smallest angular size known so far.

With deep SOAR data we found that DES J0222.7−5217 is located at a heliocentric distance of 77.3 kpc, and it hosts an old ($\simeq 12.6$ Gyr) and metal-poor ([Fe/H] $\simeq -2.01$) stellar population. Our best-fitting structural parameters for DES J0222.7−5217 are in general agreement (within 1σ) with the ones derived by Bechtol et al. (2015) and Koposov et al. (2015a), although the heliocentric distance determined in this work points to a closer object than previously reported. The half-light radius ($r_{\rm h} \simeq 11.24$ pc) and luminosity ($M_V \simeq -2.4$) of DES J0222.7−5217 suggest that it could be classified as a faint star cluster. However, spectroscopic measurements of metallicity and radial velocity of the stars of DES J0222.7−5217 will be very useful to confirm its nature, since the dynamic mass of the object is determined from the radial velocity dispersion of its stars (see e. g. Wolf et al. 2010; Willman & Strader 2012, for more details).

Based on the Magellanic Stream (MS; Nidever, Majewski & Butler Burton 2008) coordinates of DES 3, $(L_{\rm MS}, B_{\rm MS}) \simeq -37°39$, $-31°69$ and DES J0222.7−5217, $(L_{\rm MS}, B_{\rm MS}) \simeq -26°45$, $8°25$, it
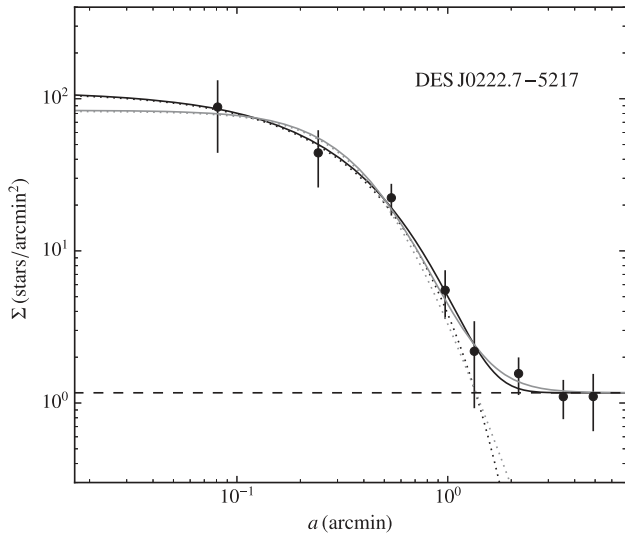
Figure 12. Elliptical surface density profile of DES J0222.7−5217. The filled points represent the observed values with 1σ error bars. The grey (black) dotted line represents the best-fitting of Plummer (exponential) profile. The horizontal dashed line represents the background density. The grey (black) solid line is the combination of the background level with the Plummer (exponential) profile.

is interesting to note that DES J0222.7−5217 is in a region where there is a high probability of finding objects associated with the Magellanic Clouds, while DES 3 lies close to a sequence of faint dwarf galaxies, some of which may also be associated with the Clouds (Fig. 10; Jethwa et al. 2016). However, DES 3 lies outside $\pm 20°$ of the plane of the MS where the satellites of the LMC would be distributed (Jethwa et al. 2016). In particular, DES J0222.7−5217 is located $\simeq 39.9$ kpc from the LMC and $\simeq 31.3$ kpc from the SMC centre, distances about (or less than) a half than the distance of DES J0222.7−5217 to the Galactic Centre ($\simeq 77.4$ kpc).

Finally, the discovery of DES 3 in DES data indicates that the census of stellar systems, with characteristics of faint star clusters, is still incomplete. It is likely that additional new stellar systems will be found in future DES data. We have demonstrated the value of deeper imaging to improve the photometric errors and to detect stars at and below the MSTO. This greatly improves the fitting of isochrones, in particular tightening the constraints on the age. For many of these newly discovered objects, a wide field is not needed and SOI on the SOAR telescope is an ideal instrument for follow-up studies.

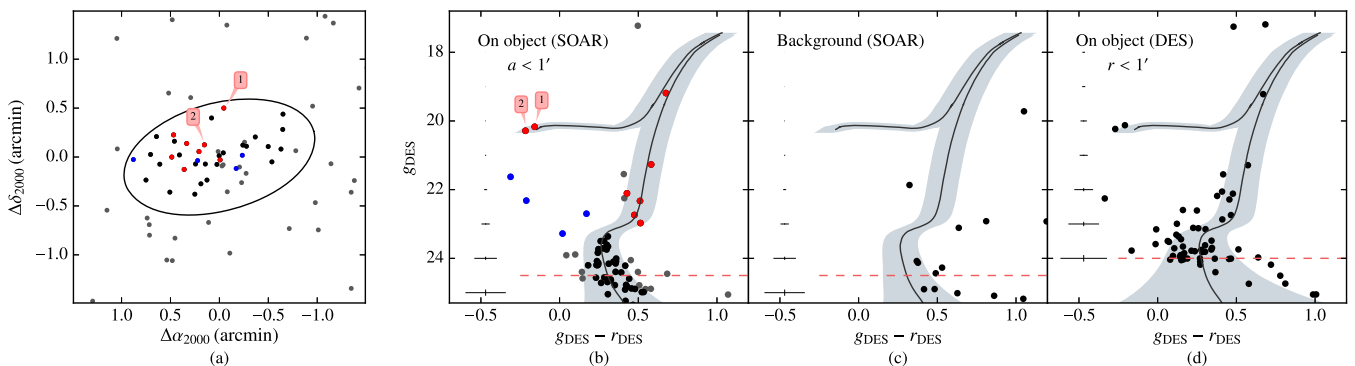**Figure 13.** Panel (a): spatial distribution of all sources classified as stars, with $g_{DES} < 24.5$, from the SOAR data in a field of view of $3' \times 3'$ centred on DES J0222.7−5217. The black dots represent the stars inside an ellipse with semimajor axis $a = 1'$ ($\simeq 2r_{h}$), $\theta = -74°.70$, and $\epsilon = 0.45$ (see Table 3), and that fall inside the isochrone filter as illustrated in the next panel. The red (blue) dots mark the RGB and HB (BS) stars. Panel (b): CMD of DES J0222.7−5217 from the SOAR data. Only stars inside the ellipse marked on panel (a) are shown. In this and the other two panels, the best-fitting PARSEC (Bressan et al. 2012) isochrone derived from the SOAR data is shown. The isochrone filter (grey shaded area) based on photometric uncertainties contains the most likely members. Panel (c): CMD of field stars in an elliptical annulus, from the centre of DES J0222.7−5217, of equal area on the sky as the previous panel. Panel (d): CMD of DES stars within a radius $r = 1'$ centred on DES J0222.7−5217. The horizontal dashed line in the last three panels indicates the faint magnitude limit used. The mean photometric errors in both colour and magnitude are shown in the extreme left of panels (b), (c), and (d).

REFERENCES

Balbinot E. et al., 2013, ApJ, 767, 101
Balbinot E. et al., 2015, MNRAS, 449, 1129
Bechtol K. et al., 2015, ApJ, 807, 50
Belokurov V. et al., 2010, ApJ, 712, L103
Bertin E., 2011, in Evans I. N., Accomazzi A., Mink D. J., Rots A. H., eds, ASP Conf. Ser. Vol. 442, Astronomical Data Analysis Software and Systems XX. Astron. Soc. Pac., San Francisco, p. 435
Bertin E., Arnouts S., 1996, A&AS, 117, 393
Bressan A., Marigo P., Girardi L., Salasnich B., Dal Cero C., Rubele S., Nanni A., 2012, MNRAS, 427, 127
Davis M., Efstathiou G., Frenk C. S., White S. D. M., 1985, ApJ, 292, 371
Desai S. et al., 2012, ApJ, 757, 83
Dooley G. A., Peter A. H. G., Carlin J. L., Frebel A., Bechtol K., Willman B., 2017, MNRAS, 472, 1060
Drlica-Wagner A. et al., 2015, ApJ, 813, 109
Drlica-Wagner A. et al., 2016, ApJ, 833, L5
Drlica-Wagner A. et al., 2018, ApJS, 235, 33
Fadely R., Willman B., Geha M., Walsh S., Muñoz R. R., Jerjen H., Vargas L. C., Da Costa G. S., 2011, AJ, 142, 88
Flaugher B. et al., 2015, AJ, 150, 150
Font A. S. et al., 2011, MNRAS, 417, 1260
Foreman-Mackey D., Hogg D. W., Lang D., Goodman J., 2013, PASP, 125, 306
Harris W. E., 2010, preprint (arXiv:1012.3224)
Homma D. et al., 2016, ApJ, 832, 21
Homma D. et al., 2018, PASJ, 70, S18
Ibata R. A., Gilmore G., Irwin M. J., 1994, Nature, 370, 194
Ibata R., Nipoti C., Sollima A., Bellazzini M., Chapman S. C., Dalessandro E., 2013, MNRAS, 428, 3648
Jester S. et al., 2005, AJ, 130, 873
Jethwa P., Erkal D., Belokurov V., 2016, MNRAS, 461, 2212
Kim D., Jerjen H., 2015a, ApJ, 799, 73
Kim D., Jerjen H., 2015b, ApJ, 808, L39
Kim D., Jerjen H., Milone A. P., Mackey D., Da Costa G. S., 2015, ApJ, 803, 63
Kim D., Jerjen H., Mackey D., Da Costa G. S., Milone A. P., 2016a, ApJ, 820, 119
Kim D. et al., 2016b, ApJ, 833, 16
Koposov S. et al., 2007, ApJ, 669, 337
Koposov S. E., Belokurov V., Torrealba G., Evans N. W., 2015a, ApJ, 805, 130
Koposov S. E. et al., 2015b, ApJ, 811, 62
Koposov S. E., Belokurov V., Torrealba G., 2017, MNRAS, 470, 2702
Kroupa P., 2001, MNRAS, 322, 231
Laevens B. P. M. et al., 2014, ApJ, 786, L3
Laevens B. P. M. et al., 2015a, ApJ, 802, L18
Laevens B. P. M. et al., 2015b, ApJ, 813, 44
Law D. R., Majewski S. R., 2010, ApJ, 718, 1128
Li T. S. et al., 2017, ApJ, 838, 8
Luque E. et al., 2016, MNRAS, 458, 603
Luque E. et al., 2017, MNRAS, 468, 97
McConnachie A. W., 2012, AJ, 144, 4
Mackey A. D., Gilmore G. F., 2004, MNRAS, 355, 504
Marino A. F. et al., 2014, MNRAS, 442, 3044
Marino A. F. et al., 2015, MNRAS, 450, 815
Martin N. F., de Jong J. T. A., Rix H.-W., 2008, ApJ, 684, 1075
Martin N. F. et al., 2015, ApJ, 804, L5
Mateo M., Olszewski E. W., Pryor C., Welch D. L., Fischer P., 1993, AJ, 105, 510
Mohr J. J. et al., 2012, in Radziwill N. M., Chiozzi G., eds, Proc. SPIE Conf. Ser., Vol. 8451, Software and Cyberinfrastructure for Astronomy II. SPIE, Bellingham, p. 84510D
Muñoz R. R., Geha M., Côté P., Vargas L. C., Santana F. A., Stetson P., Simon J. D., Djorgovski S. G., 2012, ApJ, 753, L15
Nidever D. L., Majewski S. R., Butler Burton W., 2008, ApJ, 679, 432
O'Malley E. M., Gilligan C., Chaboyer B., 2017, ApJ, 838, 162
Odenkirchen M., Grebel E. K., Dehnen W., Rix H.-W., Wolf C., Rockosi C. M., 2002, in Grebel E. K., Brandner W., eds, ASP Conf. Ser., Vol. 285, eds, Modes of Star Formation and the Origin of Field Populations. Astron. Soc. Pac., San Francisco, p. 184
Pieres A. et al., 2016, MNRAS, 461, 519
Plummer H. C., 1911, MNRAS, 71, 460
Rockosi C. M. et al., 2002, AJ, 124, 349
Sales L. V., Navarro J. F., Kallivayalil N., Frenk C. S., 2017, MNRAS, 465, 1879
Schlegel D. J., Finkbeiner D. P., Davis M., 1998, ApJ, 500, 525
Sevilla I. et al., 2011, preprint (arXiv:1109.6741)
Simon J. D. et al., 2015, ApJ, 808, 95
Simon J. D. et al., 2017, ApJ, 838, 11
Szabo T., Pierpaoli E., Dong F., Pipino A., Gunn J., 2011, ApJ, 736, 21
The Dark Energy Survey Collaboration 2005, preprint (astro-ph/0510346)
Torrealba G., Koposov S. E., Belokurov V., Irwin M., 2016a, MNRAS, 459, 2370
Torrealba G. et al., 2016b, MNRAS, 463, 712
Walker M. G., Mateo M., Olszewski E. W., Bailey J. I., III, Koposov S. E., Belokurov V., Evans N. W., 2015, ApJ, 808, 108
Walker M. G. et al., 2016, ApJ, 819, 53
White S. D. M., Rees M. J., 1978, MNRAS, 183, 341
Willman B., Strader J., 2012, AJ, 144, 76
Wolf J., Martinez G. D., Bullock J. S., Kaplinghat M., Geha M., Muñoz R. R., Simon J. D., Avedo F. F., 2010, MNRAS, 406, 1220

York D. G. et al., 2000, AJ, 120, 1579

Zinn R., 1985, ApJ, 293, 424

Zinn R., 1993, in Smith G. H., Brodie J. P., eds, ASP Conf. Ser., Vol. 48, The Globular Cluster-Galaxy Connection. Astron. Soc. Pac., San Francisco, p. 38

[1]*Instituto de Física, UFRGS, Caixa Postal 15051, Porto Alegre, RS 91501-970, Brazil*

[2]*Laboratório Interinstitucional de e-Astronomia - LIneA, Rua Gal. José Cristino 77, Rio de Janeiro, RJ 20921-400, Brazil*

[3]*George P. and Cynthia Woods Mitchell Institute for Fundamental Physics and Astronomy, and Department of Physics and Astronomy, Texas A&M University, College Station, TX 77843, USA*

[4]*Fermi National Accelerator Laboratory, P. O. Box 500, Batavia, IL 60510, USA*

[5]*Kavli Institute for Cosmological Physics, University of Chicago, Chicago, IL 60637, USA*

[6]*Department of Physics, University of Surrey, Guildford GU2 7XH, UK*

[7]*Observatório Nacional, Rua Gal. José Cristino 77, Rio de Janeiro, RJ 20921-400, Brazil*

[8]*Cerro Tololo Inter-American Observatory, National Optical Astronomy Observatory, Casilla 603, La Serena, Chile*

[9]*Department of Physics and Astronomy, University College London, Gower Street, London WC1E 6BT, UK*

[10]*Department of Physics and Electronics, Rhodes University, PO Box 94, Grahamstown 6140, South Africa*

[11]*LSST, 933 North Cherry Avenue, Tucson, AZ 85721, USA*

[12]*CNRS, UMR 7095, Institut d'Astrophysique de Paris, F-75014 Paris, France*

[13]*Sorbonne Universités, UPMC Univ Paris 06, UMR 7095, Institut d'Astrophysique de Paris, F-75014 Paris, France*

[14]*Department of Astronomy, University of Illinois, 1002 W. Green Street, Urbana, IL 61801, USA*

[15]*National Center for Supercomputing Applications, 1205 West Clark St., Urbana, IL 61801, USA*

[16]*Institut de Física d'Altes Energies (IFAE), The Barcelona Institute of Science and Technology, Campus UAB, E-08193 Bellaterra (Barcelona) Spain*

[17]*Institute of Space Sciences, IEEC-CSIC, Campus UAB, Carrer de Can Magrans, s/n, E-08193 Barcelona, Spain*

[18]*Kavli Institute for Particle Astrophysics and Cosmology, P. O. Box 2450, Stanford University, Stanford, CA 94305, USA*

[19]*Department of Physics, California Institute of Technology, Pasadena, CA 91125, USA*

[20]*Jet Propulsion Laboratory, California Institute of Technology, 4800 Oak Grove Dr., Pasadena, CA 91109, USA*

[21]*Instituto de Fisica Teorica UAM/CSIC, Universidad Autonoma de Madrid, E-28049 Madrid, Spain*

[22]*Department of Astronomy, University of Michigan, Ann Arbor, MI 48109, USA*

[23]*Department of Physics, University of Michigan, Ann Arbor, MI 48109, USA*

[24]*SLAC National Accelerator Laboratory, Menlo Park, CA 94025, USA*

[25]*Center for Cosmology and Astro-Particle Physics, The Ohio State University, Columbus, OH 43210, USA*

[26]*Department of Physics, The Ohio State University, Columbus, OH 43210, USA*

[27]*Astronomy Department, University of Washington, Box 351580, Seattle, WA 98195, USA*

[28]*Australian Astronomical Observatory, North Ryde, NSW 2113, Australia*

[29]*Institució Catalana de Recerca i Estudis Avançats, E-08010 Barcelona, Spain*

[30]*Institute of Cosmology and Gravitation, University of Portsmouth, Portsmouth PO1 3FX, UK*

[31]*Centro de Investigaciones Energéticas, Medioambientales y Tecnológicas (CIEMAT), Madrid, Spain*

[32]*School of Physics and Astronomy, University of Southampton, Southampton SO17 1BJ, UK*

[33]*Instituto de Física Gleb Wataghin, Universidade Estadual de Campinas, SP 13083-859, Campinas, Brazil*

[34]*Computer Science and Mathematics Division, Oak Ridge National Laboratory, Oak Ridge, TN 37831, USA*

This paper has been typeset from a TEX/LATEX file prepared by the author.